Divertor heat loads in RMP ELM controlled H-mode plasmas on DIII-D[*]

M.W. Jakubowski[1,2], C.J. Lasnier[4], O. Schmitz[2], T.E. Evans[3], M.E. Fenstermacher[4], M. Groth[4], J.G. Watkins[6], T. Eich[1], R.A. Moyer[5], R.C. Wolf[1], L.B. Baylor[3], J.A. Boedo[5], K.H. Burrell[3], H. Frerichs[2], J.S. deGrassie[3], P. Gohil[3], I. Joseph[5], M. Lehnen[2], A.W. Leonard[3], C.C. Petty[3], R.I. Pinsker[3], D. Reiter[2], T.L. Rhodes[5], U. Samm[2], P.B. Snyder[3], H. Stoschus[2], T. Osborne[3], B. Unterberg[2], W.P. West[3]

[1] Max-Planck-Institut für Plasmaphysik, IPP-EURATOM Association, Garching & Greifswald, Germany
[2] Institut für Energieforschung 4 – Plasmaphysik, Forschungszentrum Jülich, Association FZJ-EURATOM, TEC, Jülich, Germany
[3] General Atomics, P.O. Box 85608, San Diego, California, 92186-5608 U.S.A.
[4] Lawrence Livermore National Laboratory, P.O. Box 808, Livermore, CA 94550, U.S.A.
[5] University of California, San Diego, La Jolla, CA 92093, U.S.A.
[6] Sandia National Laboratory, Albuquerque, New Mexico, U.S.A.

Abstract. In this paper the manipulation of power deposition on divertor targets at DIII-D by application of resonant magnetic perturbations (RMPs) is analysed. It has been found that heat transport shows a different reaction to the applied RMP depending on the plasma pedestal collisionality. At pedestal electron collisionality above 0.5 the heat flux during the ELM suppressed phase is of the same order as the inter-ELM in the non-RMP phase. Below this collisionality value we observe a slight increase of the total power flux to the divertor. This can be caused by much more negative potential at the divertor surface due to hot electrons reaching the divertor surface from the pedestal area and/or so called pump out effect. In the second part we discuss modification of ELM behaviour due to the RMP. It is shown, that the width of the deposition pattern in ELMy H-mode depends linearly on the ELM deposited energy, whereas in the RMP phase of the discharge those patterns seem to be controlled by the externally induced magnetic perturbation. D_2 pellets injected into the plasma bulk during ELM-free RMP H-mode lead in some cases to a short term small transients, which have very similar properties to ELMs in the initial RMP-on phase.

1. Introduction

Type-I Edge Localized Modes (ELMs) [1] are a significant concern in tokamak plasmas. They appear as a series of rotating filamentary structures [2] due to pedestal pressure gradients found at the edge of H-mode plasmas [3]. ELMs are also responsible for spiral patterns of heat loads on the surface of the divertor [4]. They have been successfully mitigated in H-mode plasmas at the DIII-D tokamak by application of resonant magnetic perturbations (RMPs) produced by coils external to the plasma but inside the vacuum vessel over wide range of pedestal collisionalities and plasma shapes [5,6]. Currents flowing in the coils impose three-dimensional structure of the stochastic magnetic field lines in the plasma edge [7,8]. This is a result of interaction of the RMP with plasma magnetic equilibrium, which imposes a perturbed volume into the plasma boundary. Topologically, this volume consists of two layers. The inner stochastic boundary, where presumably radial particle transport is enhanced due to high diffusivity of magnetic field lines, is located near the pedestal area. At the separatrix a set of invariant manifolds is created, which forms a specific spiral pattern on the divertor surface. Lobes of the manifolds form an envelope for the open field lines leaving the stochastic area and intersecting the divertor target plates [9]. In this paper we review the results of heat flux behaviour with the $n = 3$ RMP and compare them to non-RMP H-mode results for a wide range of pedestal collisionalities $\nu_{\mathrm{ped}}^* = q_{95} R \varepsilon^{-3/2} \lambda_{\mathrm{ee}}^{-1}$ at

high and low triangularity (including ITER-similar shapes). Here R is the major radius of the torus, $\varepsilon \equiv a / R$ inverse aspect ratio and λ_{ee} – mean free path for electron collisions.

2. Experimental set-up

For the experiments discussed in this paper, we examine both near double-null plasma discharges at high collisionality with moderate to high triangularity (magnetically shifted slightly down) and also lower single null plasmas with low density, low collisionality (both low and high triangularity). They had slight variation in q_{95} in order to stay in the resonant window for magnetic perturbation, in which Type-I ELMs are completely suppressed [5]. The preferred diagnostic for divertor target heat load measurements is infrared thermography. In this work the heat flux analysis has been performed with two infra-red cameras mounted at two different toroidal locations: 1) a fast-framing infra-red Santa Barbara Focal Plane (SBFP) camera at toroidal angle of ($\varphi = 165°$) with time resolution of 13 kHz and spatial resolution of few millimetres per pixel on the target surface, and 2) the FLIR Systems Inc. infra-red camera located at toroidal angle ($\varphi = 60°$) with 50 Hz time resolution and similar spatial resolution. Both cameras have a line of sight observing the lower divertor area; however in most cases they did not run simultaneously. The heat fluxes on the target surfaces are calculated for the SBFP system by applying a standard numerical solution of the two-dimensional heat diffusion equations to the evolution of the surface temperature on the investigated area [10] while for the FLIR system a semi-infinite approximation for the heat diffusion in a solid bulk material.

## 3. Heat flux to the divertor at different collisionalities

The heat flux data presented in this section is recorded with time resolution of 50 Hz, which makes it impossible to resolve details of heat loads for each individual ELM. The high- and low-collisionality discharges show different behaviour of the heat flux to the divertor during ELM suppression. This is presented in Figure 1a, where time traces for #119692 ($\nu^*_{\text{ped}} \approx 3 - 4, \quad q_{95} = 3.7$) and #126006 ($\nu^*_{\text{ped}} \approx 0.3, \quad q_{95} = 3.5$) are presented. Both discharges are high triangularity discharges with upper and lower triangularity of ($\delta_{\text{up}} = 0.4, \delta_{\text{low}} = 0.6$) and ($\delta_{\text{up}} = 0.3, \delta_{\text{low}} = 0.7$) respectively. In both cases the I-coils have been run with almost the same current of 4 kA. In the high collisionality case (black curves) ELMs are suppressed immediately after I-coils are switched on ($t = 3000$ ms). There is no significant effect on the energy deposited to the target plates of the lower divertor. As the diamagnetic energy is not affected by stochastization of the plasma boundary, there is also no temporary increase of the deposited energy due to heat pulse crossing the separatrix. As reported in [11] at high collisionality, the floating potential (V_f) measured by the divertor Langmuir probes near the outer strike point is approximately zero during application of the RMP, suggesting a drop of the temperature in the scrape-off layer and weaker acceleration of ions towards the target by the sheath due to RMP application. For discharge #119692, the floating potential evenly increases from slightly above 0V to a few volts as shown in Figure 1b, black curve. However, contrary results are obtained for low collisionality discharges (e.g. #126006) – ELM suppression by the RMP is associated with the density pump-out and a small drop of the diamagnetic energy. As the confinement drops there is an additional portion of energy leaving the plasma, what is immediately seen as a 50 % increase of the total heat flux to the divertor. After the energy confinement returns to the equilibrium value, the energy deposited to the divertor remains on a higher level as compared to the non-RMP phase.
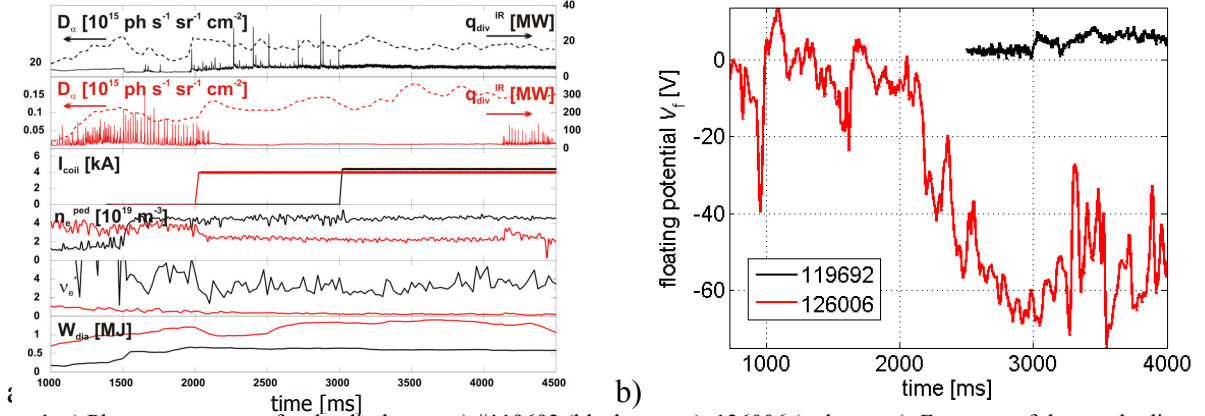
Figure 1. a) Plasma parameters for the discharges a) #119692 (black curves), 126006 (red curves). From top of the graph: divertor particle (solid) and heat flux (dashed) on top two graphs, I-coil current, pedestal electron density, pedestal collisionality, plasma stored energy. b) Floating potential measured by the Langmuir probe near the outer strike point for the same discharges.

This increase of the heat flux is typical for all low pedestal collisionality discharges at DIII-D. However, already at $\nu_{\mathrm{ped}}^* \gtrsim 0.5$ the power deposited to the target is not affected by the application of RMP. This is accompanied by the fact that the floating potential at the position of the strike point becomes strongly negative as illustrated in Figure 1b. These findings suggest interaction of the hot electrons with the surface of the target plates. Most likely these electrons come from the pedestal area along the magnetic field lines perturbed by the RMP and at low ν_{ped}^* they are almost collisionless. Conversely, at the collisionality of 3 or 4 they are not able to reach from the pedestal to the sheath area, i.e the hot electrons are more eligible to dissipate energy before reaching the surface of the targets.
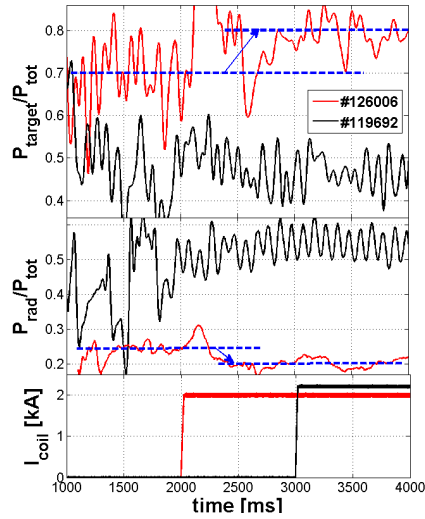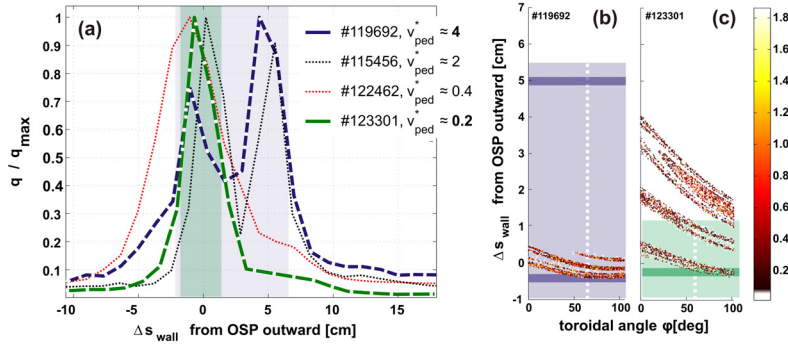

Figure 2. Power balance for the high (blue) and low collisionality discharges: (topmost) ratio of the power deposited to the target and the total heating power, (middle) ratio of the radiated power to the total heating power, (bottom) I-coil current

More negative floating potential enhances transfer of the energy to ions and thus increase of the heat flux to the surface. Figure 2 illustrates changes in the power reaching the divertor (P_{target}) and the radiated power (P_{rad}) normalized to the total heating power (P_{tot}) when the I-coils are energized. The power to the target is obtained using the equation: $P_{\mathrm{target}} = P_{\mathrm{tot}} - P_{\mathrm{rad}} - \mathrm{d}W_{\mathrm{dia}}/dt$, where W_{dia} is the diamagnetic stored energy. The power balance has been performed based on the 1D traces, owing more careful analysis for the future Nuclear Fusion paper, which will follow this contribution. Nevertheless, already for all the cases, where inner and outer legs could be observed by the infrared camera, there was very good agreement between P_{target} and power to the divertor measured by the camera. At low collisionality, before the RMP phase, about 70% of the total energy is deposited to the target. This amount is increased by about 15% (to 80% of total heating power) after the I-coils are energized; at the same time radiated power drops from 25% to 20% of P_{tot}. The situation looks different at higher collisionality – there both P_{target} and P_{rad} exhaust similar fraction of energy, which is not affected by the RMP. Probably, the pre-RMP ratio of P_{rad} and P_{target} in low

collisionality discharges can be maintained during the RMP phase by seeding of a small fraction of impurities, which would enhance radiation in the divertor area.

As mentioned already in Section 1, application of any non-axisymmetric perturbation removes degeneration of the separatrix manifolds, what is often referred to in the literature as a splitting of the strike line. It has been reported previously [7] that the particle flux, contrary to the heat flux, almost always creates measurable signature of the perturbed strike line striation. For the discharges investigated in this work, we observe that the structure of the heat flux profiles on the divertor surface changes with the pedestal collisionality. Figure 3.a shows profiles of normalized heat flux density measured at the location of the outer strike point during the RMP phase at four different pedestal collisionalities. It is apparent that at high ν^*_{ped} an additional lobe of the strike zone appears, when the $n = 3$ perturbation is applied. It has been found that only there is a clear splitting of the separatrix visible in the heat flux at high collisionalities ($\nu^*_{\mathrm{ped}} > 2$). However, as discussed in [8] the separation of the lobes is 2-3 times larger than anticipated by the TRIP3D calculations [12] depicted for the high ν^*_{ped} case (#119692) in figure 3b and for the low ν^*_{ped} case in figure 3c. Here, only very small heat fluxes [10] and in the actual example no heat flux at all is seen to be channeled along the perturbed separatrix lobes although they are separated by a rather huge distance of 1.5 cm each (see figure 3c). These results suggest that the plasma response to the applied $n = 3$ edge resonant magnetic perturbation may amplify the effects of the external perturbation in terms of perturbation of the separatrix manifolds. This has two effects on the power deposition pattern to the divertor:


Figure 3. a) Profiles of the heat flux density at different levels of collisionality at the toroidal angle of φ = 60°. The abscissa represents distance from the separatrix, the ordinate normalized heat flux density. Second lobe of the splitted separatrix appears at $R - R_{\mathrm{sep}} \approx 5 - 6\mathrm{cm}$. Structures of the outer strike point as predicted by TRIP3D for 123301 **b)** and 119692 **c)**. Here, also the measurement position is indicated by the white, dashed line and the profile width (FWHM) is marked as shaded box while the peak position is included as solid line for both discharges modeled.

a. Amplification of the separatrix deformation, i.e. larger splitting of the strike line than predicted from the vacuum magnetic field modeling.
b. Possible enhanced coupling of the outer lobes to the pedestal by deeper penetration of magnetic field lines, which results in higher heat deposited through the outer lobes. One should note, that enhanced heat flux in the outer lobe also happens during discharges affected by locked modes in the plasma core and (as discussed in the next section) during ELMs.

At lower collisionalities (e.g. #123301) the width of the heat flux profile (~ 5 cm) corresponds roughly to the structure of the outer strike point (figure 3.c) calculated by the TRIP3D code, which has about 3 cm width at φ = 60°. As the thermographic system has spatial resolution of order 1 cm, it is not possible to evaluate the internal structure of the strike point. However, recent measurements [7] with higher spatial resolution show that the outer lobe of the inner strike line during discharges with $\nu^*_{\mathrm{ped}} \approx 0.2$ can be resolved experimentally, but with a low amount of the heat deposited there.

4. Influence of RMP on ELM deposition patterns

In this section we use the high time resolution (13 kHz) of the SBFP camera system to resolve the ELM structure during RMP application. It has been reported from ASDEX-Upgrade, that Type-I ELMs create helical footprint patterns of heat flux on the divertor surface [4]. Several strike lines were detected outside the original strike point of the outer leg albeit at very low amplitude. They form helically aligned structures, which are clearly related to the topology of the magnetic field. In this work we have found very similar structures on the inner and outer target plates. However, as most of the area of the outer strike point is hidden from the infrared camera by the vessel structures, we will concentrate on the substructures detected during ELM events on the inner target plates of an H-mode discharge. The investigated discharges have been performed at low pedestal collisionality ($\nu^*_{\mathrm{ped}} \approx 0.3$) and ITER-like plasma shapes ($\delta_U = 0.32, \ \delta_L = 0.70$). An example of the scenario is given in figure 4a.

(a)   **(b)**   **(c)**
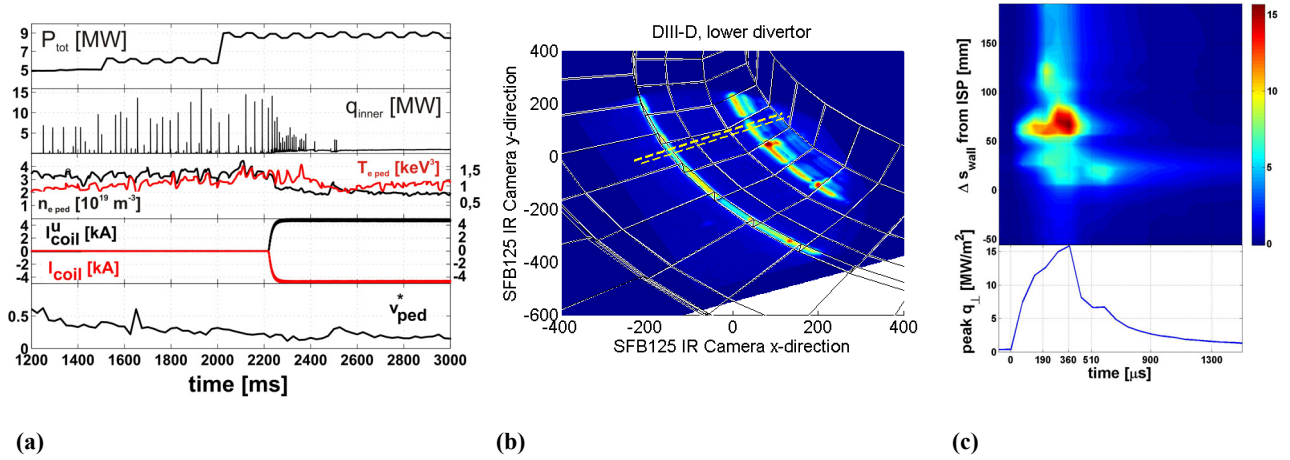
Figure 4. a) Time traces for discharge #129197 (from top to bottom): total heating power, power flux to the inner divertor; pedestal electron density and temperature; I-coil currents; pedestal collisionality. **b)** example of an infared image of the divertor surface during Type-I ELM. Yellow dashed lines indicate area, where heat flux density is evaluated. **c)** evolution of the heat flux density at the inner strike point during Type-I ELM: (top) contour plot of heat flux density evolution at the inner strike point in false color representation (units in MW/m^2); (bottom) peak heat flux density vs. time for the same event.

At $t \approx 1200$ ms there is a transition to ELMy H-mode associated by a mixture of large Type-I ELMs with frequency of about 50 Hz and small ones (probably Type-II ELMs). Switching on the I-coil current of 4.5 kA at first makes ELMs more frequent (~200 Hz) and changes their amplitudes. Peak heat flux due to Type-I ELMs decreases roughly by factor of 3 and due to Type-II increases by factor of 2. Shortly before t = 2400 ms all instabilities disappear completely. Small ELM-like bursts at t $\approx$ 2500 ms are caused by pellets injected into the plasma. They have amplitudes of the same order as ELMs in the initial RMP phase, i.e. much smaller than the ELMs without the RMP. An example of an infrared image taken by the SBFP camera of the substructures during an ELM without the RMP is shown in figure 4b) and 4c) Three additional strike lines are visible in the remote area of the inner strike line (upper, right part of the image). Usually, there are two to five non-axisymmetric strike lines observed at the location of the inner strike line during an ELM event. Their width is typically in the range of $2 - 4$ cm and the separation between them of the same order. The grid embedded onto the image shows the vessel model applied in the LEOPOLD code [4] to unfold the temperature data. Heat flux density is calculated using the THEODOR code [10], which has the ability to evaluate the influence of the co-deposits on the evaluated heat flux density.
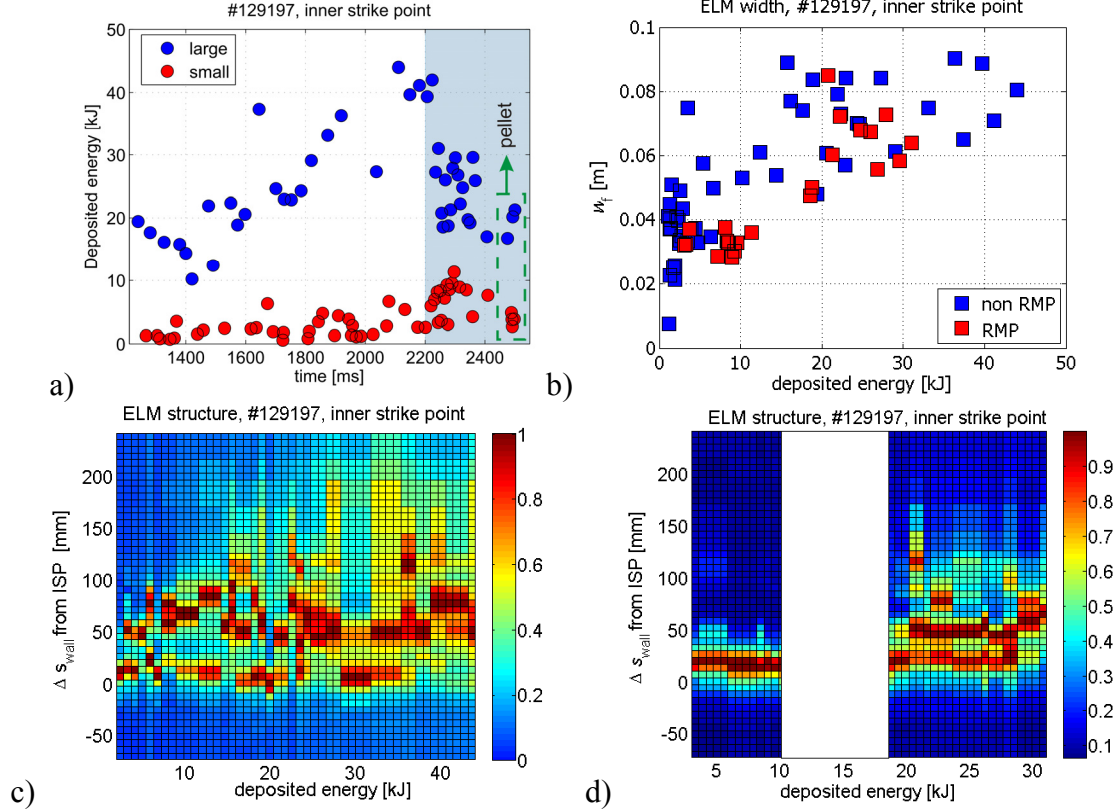
Figure 5. Properties of ELMs during ITER similar shape (ISS) discharge at low pedestal collisionality. **a)** Energy deposited to the inner divertor target by Type-I (blue circles, reduced by factor of 2 in RMP phase) and Type-II (red circles) ELMs, RMP phase is indicated as light blue box. **b)** Width of an ELM profile at maximum: blue squares (non-RMP phase), red squares (RMP phase). Profiles of ELM heatflux normalized to the peak heat flux value during non-RMP phase **c)** and during initial RMP phase **d)**, where two groups of ELMs can be distinguished by the deposited energy (each vertical line corresponds to one ELM event). Therefore no ELMs at all exists in the energy range inside of the white box..

For the purpose of this work we have performed calculations in the area indicated by two yellow dashed lines. Temperature data have been obtained with very good time resolution (f = 13 kHz), which allowed the evolution of the structures during an ELM event to be seen. An example is shown in figure 4.c. At the ELM onset (t = 1961 ms, #129197) two strike lines appear (at $s − s_0 \approx$ 20 mm and $s − s_0 \approx$ 60 mm) with the latter one depositing most of the heat to the target. At a time 190 μs later, the third substructure (at $s − s_0 \approx$ 120 mm) appears and last only until heat flux deposition gets to its maximum at Δt = 360 μs. After another 150 μs the second lobe disappears rather rapidly. For some of the ELM events there is a clear signature of the lobes separation, which suggests toroidal rotation of the structures. Total energy deposited to the target during this event is about 39 kJ.

The energy deposited to the inner target per ELM versus time for all investigated ELMs is presented in Figure 5Figure a. There is a clear distinction between two groups marked with blue and red circles. These are identified as Type-I and probably Type-II ELMs respectively (however this needs more careful stability analysis, which will be performed in the following this contribution journal article). The latter ones, as expected, deposit much smaller energy to the inner target (below 10 kJ). Before the RMP phase (t < 2200 ms) one observes an increasing amount of energy deposited to the target per ELM for 1200 ms < t < 2100 ms. This is caused by increasing heating power from the neutral beam injection, which reaches maximum of 9 MW at t ≈ 2100 ms. At this time the energy deposited per ELM reaches 40 kJ for Type-I and few kJ for

Type-II ELMs. Application of RMP at t = 2200 ms reduces the amount of energy deposited per event for Type-I ELMs to the value in the range of 20 – 30 kJ. Surprisingly, Type-II ELMs deposit more energy with the magnetic perturbation (5-10 kJ) than without the RMP. Bursts caused by the injection of D$_2$ pellets recreate both types of ELMs for a short period of time at t ≈ 2500 ms. In this shot they deposit the power to the divertor in the same ranges as ELMs in the initial RMP phase and will be discussed in the last paragraph of this work.
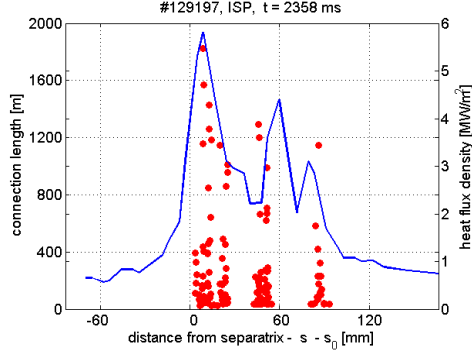
Figure 6. Comparison of heat flux deposition pattern (blue curve, right ordinate) with predicted by TRIP3D connection length distribution (red dots, left ordinate).

It is expected that ELM filaments carry some amount of current either due to a difference in the temperature between the inner and outer strike point and/or due to different inertia of very fast electrons and ions [13,18]. As the filaments have helical forms, their currents should create a magnetic perturbation, which also has components that are resonant to the edge magnetic equilibrium [13,15]. It has been shown that divertor heat flux and particle recycling patterns are consistent with magnetic footprints produced by separatrix splitting associated with homoclinic tangles under some conditions [7]. Since homoclinic tangles result naturally from a variety of stationary and/or time dependent non-axisymmetric magnetic perturbations that are found in any realistic tokamak, it is not unreasonable to expect these structures to be the norm rather than the exception whether in an L-mode or H-mode as well as between ELMs and during the on-set of an ELMs. These components should create temporal ergodization of the separatrix, which is consistent with the observed splitting of the separatrix during ELMs. Intuitively, one would expect that larger ELMs should carry larger currents, which would eventually lead to the greater splitting of the separatrix than for the small ones. This is actually consistent with the experimental findings as presented in 5 b-c. The effective width of an ELM deposition pattern is defined as $w_f = \int q(s)ds \cdot [\max(q(s))]^{-1}$ [m], where q [MW/m^2] is heat flux density profile taken at the time, when the heat load to the divertor reaches its maximum, s [m] – is the coordinate along the divertor contour, $\max(q(s))$ denotes maximum of the heat flux density profile. Dependence of w_f on ELM size (expressed as a function of deposited energy – E_{dep}) is shown in Figure 5b. There is a clear increase of the effective width versus the amount of the energy deposited per ELM from about 4 cm for Type-II ELMs (< 10 kJ) to about 8 cm for the largest Type-I ELMs. This increase seems to have a linear characteristic and the values are slightly smaller than the profile widths at the half-maximum. Profiles of deposited power for different ELMs are presented in 5c. They are ordered according to the energy deposited to the target (the abscissa) and normalized to the maximal value for each of the profiles. Here again, one recognizes increasing width of the deposition pattern with the ELM size. It is interesting to note that for virtually all ELMs below 15 kJ there are two substructures visible. Their splitting increases from 3 cm at E_{dep} = 2-3 kJ to 8 cm at E_{dep} = 15 kJ. Larger instabilities show more random structuring, with 2 to 4 or even 5 substructures. This variability is caused most like by a
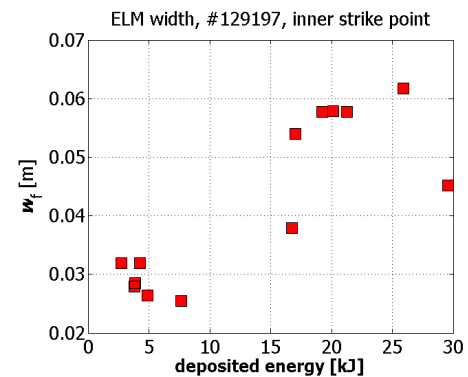
Figure 7. Effective width versus deposited energy for ELM-like bursts during D$_2$ pellet injection.

different toroidal phase of the footprint at the moment of detection and/or different shape of the perturbation spectrum.

A very interesting change in ELM behavior happens, when the $n=3$ RMP is established (red dots in figure 5b). Both types of ELMs became more similar in width ($w_f \approx$ 3-4 cm and 7 cm respectively) and narrower, when compared to the same energies in the non-RMP case. Their structure became almost the same – all instabilities with energy deposited below 15 kJ do not have any additional substructure. Almost all above 20 kJ have three deposition lobes with the distance along them not varying with the energy. This probably means that structure of the separatrix is dominated by the magnetic perturbation coming from the I-coils, i.e. that the radial magnetic component of the magnetic field induced by 4 kA I-coil current is much stronger, than b_r induced by currents flowing within the filaments. Indeed, the measurements performed on TEXT have shown that filaments can carry currents of order of hundreds of Amperes [13], which is a small fraction of 4 kA. The heat pulse due to ELMs travelling across the separatrix is diverted along the open field lines of the stochastic boundary to the target plates and deposited through the lobes of the separatrix. Figure 6 shows a comparison of the measured heat flux density profile with predictions of the structure of target patterns from TRIP3D. If we compare the deposition profile of Type-I ELM with the topology of magnetic footprints we find fair agreement between both structures. This is consistent with the hypothesis presented above.

As has been stated in the beginning of this section, injection of D_2 pellets into the plasma can in some cases cause the appearance of ELM-like bursts. If we calculate again the effective width (w_f) and plot it against deposited energy (E_{dep}), as it is presented in Figure 7, we find a similar picture, which has been found for the initial RMP phase (figure 5.b). There are two clouds of dots: the first one at (E_{dep} = 5 [kJ], $w_f \approx$ 0.03 [m] and the second at E_{dep} = 20 – 25 [kJ], $w_f \approx$ 0.05 – 0.06 [m]). However, one should note, that there are discharges, where injection of pellets during the RMP phase causes only the appearance of the smaller events of these two groups [14]. This similarity suggests that these instabilities are Type-I and Type-II ELMs, which are re-established for the short period of time after the pellet is injected.

5. Bibliography

[1] ZOHM, H., *Plasma Physics and Controlled Fusion* **38** (1996) 105-128
[2] KIRK, A., et al., *Physical Review Letters* **96** (2006) 185001-4
[3] WAGNER., F., et al., *Plasma Physics and Controlled Fusion* **48** (2006) A217-A239
[4] EICH, T., et al., *Plasma Physics and Controlled Fusion* **47** (2005) 815-842
[5] FENSTERMACHER, M. E., et al., *Physics of Plasmas* **15** (2008)
[6] EVANS, T. E., et al., *Physical Review Letters* **92** (2004) 235003
[7] SCHMITZ, O., et al., *Plasma Physics and Controlled Fusion* **in press**
[8] EVANS, T. E., et al., *Journal of Nuclear Materials* **363-365** (2007) 570-574
[9] EVANS, T.E., "*Implications of Topological Complexity and Hamiltonian Chaos in the Edge Magnetic Field of Toroidal Fusion Plasmas*", Singapore: World Scientific Press (2008)
[10] HERRMANN, A., et al., *Plasma Physics and Controlled Fusion* **37** (1995) 17-29
[11] WATKINS, J. G., et al., *Journal of Nuclear Materials* **363 - 365** (2007) 708 - 712
[12] EVANS, T. E., MOYER, R. A., MONAT, P., *Physics of Plasmas* **9** (2002) 4957-4967
[13] EVANS, T. E., et al., *Journal of Nuclear Materials* **220-222** (1995) 235-239
[14] EVANS, T. E., et al., 22nd IAEA Fusion Energy Conference, Geneva (2008) EX4/1
[15] EVANS, T. E., et al., *Journal of Nuclear Materials* (2008) **submitted**